Cathodic corrosion

Hersbach, T.J.P.

5

Operando HERFD-XANES Investigation of Pt during Cathodic Corrosion

Cathodic corrosion is a chemical etching phenomenon that likely occurs by forming a metal-containing anion. Though such an anion would be consistent with all experiments of cathodic corrosion, there is currently no direct evidence for its existence. The current chapter aims to provide this evidence by using X-ray absorption spectroscopy (XAS). XAS will be used to characterize platinum nanoparticles during cathodic corrosion in 10 *M NaOH. The chemical state of these particles is characterized using the X-ray absorption near edge structure (XANES), which is recorded in the high-energy resolution fluorescence detection (HERFD) configuration. This experimental design can detect small changes in the Pt sample during corrosion. These changes are quantified and compared to theoretically simulated X-ray absorption spectra. This analysis supports the existence of* Na_2PtH_6 *during cathodic corrosion. As such, the presented work provides experimental results that indicate the nature of the enigmatic cathodic corrosion immediate. In addition, the current results are, to our best knowledge, the first measurements indicating the generation of ternary metal hydrides in water.*

5.1 Introduction

Cathodic corrosion is a chemical process that dramatically etches surfaces of many metals.[1–4] Though this enigmatic phenomenon has been the subject of persistent fundamental characterization efforts, its underlying reaction mechanism is still unknown. An important reason for this lack of understanding is the short-lived nature of the main reaction intermediate. This reaction intermediate cannot be isolated for *ex-situ* characterization; instead, only cathodically corroded metallic surfaces (Chapter 2–4) or the metal (oxide) nanoparticle products of cathodic corrosion have been studied.[2,5–9] To characterize the elusive reaction intermediate, it is therefore imperative to use *operando* techniques that probe the intermediate while it is being generated during cathodic corrosion.

This chapter will form the basis of a manuscript that will be submitted to a peer-reviewed scientific journal.

Typical *operando* or *in-situ* characterization techniques rely on spectroscopy to probe either the oxidation state or chemical environment of a sample. In the present case, this would allow for identifying whether the corroding species resembles a metallic anion or perhaps a ternary metal hydride, as suggested in Chapter 4. However, many spectroscopic techniques are incompatible with the challenging electrode environment during cathodic corrosion.

For example, a technique such as Fourier-transform infrared spectroscopy (FTIR) can detect adsorbed species like hydrogen,[10] but it is generally incompatible with hydrogen bubbles that form during cathodic corrosion.[11] Hydrogen bubbles are less problematic for techniques such as surface-enhanced Raman spectroscopy (SERS), but bubble-compatible SERS requires the use of atomically thin metallic layers that will likely degrade quickly during cathodic corrosion.[12,13] A third spectroscopic technique is Mössbauer spectroscopy, which can detect oxidation state changes of elements such as gold,[14] but cannot detect dissolved species such as the species of interest during cathodic corrosion.[15]

A more suitable spectroscopic technique for studying cathodic corrosion is X-ray absorption spectroscopy (XAS).[16] XAS and, more specifically, X-ray absorption near edge structure (XANES) experiments can generate a wealth of information on both the oxidation state and presence of adsorbates of the sample of interest: *in-situ* XANES studies of Pt samples have previously been used assess the Pt d-band filling, Pt oxidation state and the presence of adsorbed species like *H, and *CO.[17–21] XANES can also be used during electrochemical measurements if the experimental setup is carefully designed.[22–26]

Operando XANES is therefore used in this chapter to study Pt nanoparticles during cathodic corrosion. These experiments are carried out in a flow cell, to reduce interference by bubble formation during experiments. Furthermore, the experiments are performed in the high-energy resolution fluorescence detection (HERFD) configuration, which significantly improves important features in the XANES spectrum.[21,26] In doing so, we can detect a subtle shift in the absorption edge position and decrease in white line intensity during cathodic corrosion. Further analysis of these spectral changes and theoretical modeling of XANES spectra suggests the existence of Na_2PtH_6 during cathodic corrosion. Though definitive proof of Na_2PtH_6 during cathodic corrosion requires further theoretical and experimental efforts, the results presented here support the “ternary metal hydride” hypothesis for cathodic corrosion.

5.2 Materials and methods

5.2.1 *Operando* XANES measurements

Operando HERFD-XANES experiments of the platinum L_{III} edge were carried out at beamline 6-2 of the Stanford Synchrotron Radiation Lightsource (SSRL). At this beamline, the incoming photon beam was passed through a double-crystal Si(311) monochromator. After the monochromation, the beam was reflected by a Rh-coated mirror. This parabolic mirror rejected harmonic photons from the beam and focused the beam onto the sample with a beam height of 420 μm full width at half maximum (FWHM) and a beam width of 129 μm FWHM. The incoming beam and the sample were aligned in grazing incidence, with the electric field vector of the beam parallel to the sample surface. The beam energy was calibrated before measurements with respect to a metallic Pt foil; for calibration, the first inflection point of the Pt L_{III} edge was assigned a value of 11563.7 eV.

After absorption of the X-rays by the sample, the fluorescent Pt $L_{\alpha 1}$ X-rays with an energy of 9442 eV were detected with a Johann-type X-ray spectrometer.[27] These X-rays were selectively diffracted onto the X-ray detector by using the (660) Bragg reflection of five Ge(110) crystals with a radius of curvature of 1 m. This setup had a combined monochromator and detector resolution of 1.0 eV.

5.2.2 Electrochemical XANES cell

For the *operando* XAS measurements, a home-made flow cell was used. In this cell, displayed in Fig. 5.1, the working electrode was the lowest point, such that the incoming beam (shown in red) could hit the sample unimpaired. Similarly, the detected outgoing Pt $L_{\alpha 1}$ X-rays (shown in grey) were able to travel towards the detector without hitting parts of the cell. More detailed descriptions and schematic drawings of the cell are given in Appendix B.

The working electrolyte was 10 M NaOH (Merck, Suprapur), which was stored in a fluorinated ethylene propylene (FEP) bottle and pumped into the cell through perfluoroalkoxy alkane (PFA) tubing. The electrolyte was pumped through the cell with a peristaltic pump (Ismatec IP-N), which was fitted with $\varnothing = 3.17\ mm$ phthalate-free polyvinyl chloride (PVC) tubing and operated at a flow rate of 10 $mL \cdot min^{-1}$.

Within the cell channel, a thin Pt (Mateck, 99.9%) counter electrode strip was placed alongside the working electrode and a Gaskatel 'HydroFlex' reversible hydrogen electrode (RHE) was placed downstream from the working electrode. The working electrode

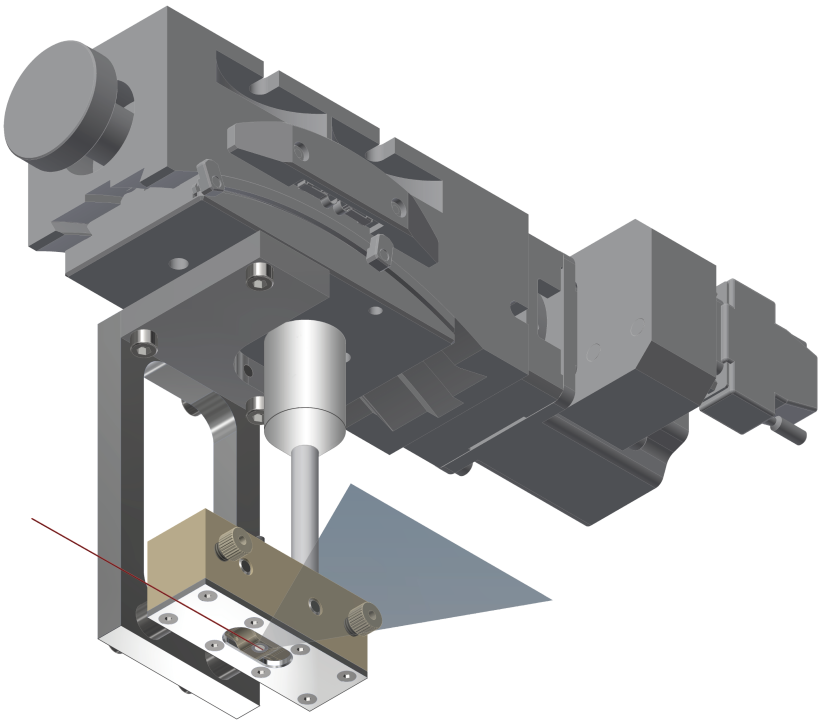

Fig. 5.1 | Schematic view of the *operando* XANES cell. The ingoing X-ray beam is indicated by the thin red line, while the detected outgoing fluorescent X-rays are visualized in grey.

consisted of a $\varnothing = 3\ mm$ gold (Alfa Aesar, 99.9985%) disk. The electrode contained a $22.5\ \mu g$ loading of surfactant-free Pt nanoparticles, which was drop-casted onto the electrode from a $0.5\ mg \cdot mL^{-1}$ solution in water. These nanoparticles were dried under a helium stream.

5.2.3 Nanoparticle preparation

The nanoparticles were prepared through cathodic corrosion,[2] by applying a 100 Hz square wave potential with $-5V/+2V$ *vs.* RHE potential limits. This potential program was 85% IR corrected and applied by a Bio-Logic SP-300 potentiostat (connected to a $2A/30V$ booster board), using a HydroFlex RHE electrode (Gaskatel) and a graphite rod (Alfa Aesar, Ultra "F" purity) counter electrode. The corrosion electrolyte was $5\ M$ KOH (Sigma-Aldrich, 99.99% trace metals basis), held within an FEP container. Using this configuration, a $\varnothing = 0.1\ mm$ Pt wire (Mateck, 99.99%) was immersed for 1 mm and cor-

roded until the entire wire was consumed. This step was repeated twice, after which the nanoparticles were purified through ultracentrifugation: the particles were centrifuged and the supernatant was replaced with clean water. The latter step was repeated until the supernatant pH was neutral.

5.2.4 Cleaning and experiment preparation

The abovementioned electrochemical setups were cleaned by storing the relevant parts overnight in a solution of $1\ g \cdot L^{-1}$ $KMnO_4$ (Fluka, ACS reagent) and $0.5\ M$ H_2SO_4 (Fluka, ACS reagent). This solution was removed before experiments, and any $KMnO_4$ residues were decomposed with dilute H_2O_2 (Merck, Emprove exp). This solution was then also removed, after which the parts were boiled five times in water. All water used in this work (resistivity $> 18.2\ M\Omega \cdot cm$, TOC $< 5\ ppb$) was cleaned using a Millipore MilliQ system. During *operando* experiments, all potentials were 85% IR corrected and applied by a Bio-Logic SP-300 potentiostat. Use of a booster board was not necessary.

5.2.5 Data processing and normalization

Using the aforementioned cell and preparation procedure, X-ray absorption spectra could be measured during electrochemical experiments. Low-noise spectra were achieved in absence of gas evolution on the working electrode, such that only four spectra needed to be recorded and averaged to yield the presented spectra. More spectra were recorded during significant gas evolution ($-0.4\ V$ *vs.* RHE and below), to compensate for noise due to bubble formation and breaking. If bubble formation led to anomalous features in spectra, these spectra were eliminated from the analysis; about 8 scans were averaged per applied potential to yield the presented data. In total, two samples, denoted sample 1 and 2 were measured at various potentials. Though both samples yielded qualitatively similar data, sample 1 is the one presented here because its spectra contained the least bubble-induced noise.

Data alignment was performed to account for shifts in the monochromator position during experiments. This was done in IgorPro by shifting the crystal glitch position to a known value. The spectra were subsequently averaged, flattened and normalized by setting the edge jump to one in ATHENA.[28] To explicitly express this normalization, all absorption spectra are plotted in y-axis units of 'edge fraction', where a value of one equals the edge jump.[16]

5.2.6 Theoretical modeling of X-ray absorption spectra

Calculations of the core edge spectroscopy were performed within the OCEAN package.[29,30] This first principles code generates X-ray absorption spectra based on both ground-state density functional theory (DFT) and the numerical solution of the Bethe-Salpeter equation (BSE) within a basis of electron and hole states (and associated core-hole dielectric screening) provided by the DFT Kohn-Sham orbitals.[31,32] The DFT electronic structure was calculated within the generalized gradient approximation using the Quantum ESPRESSO code,[33] and the BSE equation was solved with the NBSE program.[30] Efficient numerical sampling of the Brillouin zone was enabled through the use of the Shirley interpolation scheme.[34] The DFT plane-wave basis cut-off energy was set to 100 Ry using the Perdew-Berke-Ernzerhof (PBE) functional within the generalized gradient approximation (GGA).[35,36] The final states were included up to an energy range of 150 eV. The k-points used in the calculations were $12 \times 12 \times 12$, $12 \times 12 \times 12$, $6 \times 6 \times 6$, and $6 \times 6 \times 6$ for bulk Pt metal,[37] α-PtO_2,[38] Na_2HPt_4,[39] and Na_2HPt_6,[40] respectively. The real-space mesh for the BSE calculation was $12 \times 12 \times 12$, $12 \times 12 \times 12$, $6 \times 6 \times 6$, and $6 \times 6 \times 6$ for bulk Pt metal, α-PtO_2, Na_2HPt_4, and Na_2HPt_6, respectively. The radius of the sphere in which the local basis is calculated was set to $5\ Bohr$ to construct the PAW-style optimal projector functions (OPF). The screening of the core-hole interaction was done in real space using the random phase approximation up to a radius around the core of $5\ Bohr$.[41] The calculated Pt L_{III} edge spectra were numerically broadened via convolution with a Lorentzian with a half width at half maximum (HWHM) of 1.3 eV to match the broadening obtained from the HERFD mode utilized in the XAS experiments. The core-level shift was obtained through calculations for the Pt metal and then applied to the other Pt compounds. The simulated spectra were normalized with ATHENA.[28] Then, a single constant energy shift was applied to these simulated spectra to align them with the experimental data. Specifically, the calculated Pt spectrum was shifted to have the first inflection point match that of the experimental spectrum at a potential of 0.4 V *vs.* RHE: 11564.4 eV. The absolute shift to achieve this value was then applied to the other calculated spectra.

5.3 Results and discussion

In this section, we will first present X-ray absorption spectra of Pt nanoparticles at both cathodic and anodic potentials. We will then analyze these spectra qualitatively through the use of difference spectra and quantitatively by peak fitting. The spectra will then be

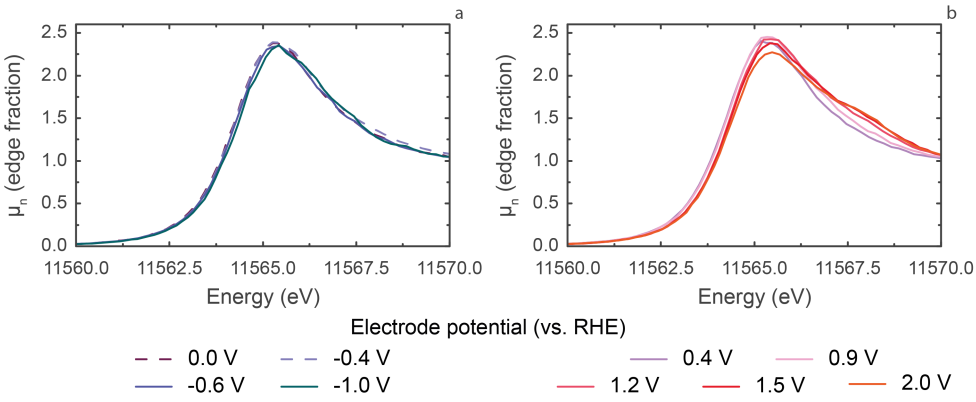

Fig. 5.2 | HERFD-XANES spectra of electrodes polarized at cathodic potentials **(a)** and anodic potentials **(b)**.

compared to modeled spectra of ternary metal hydrides, which we consider plausible reaction intermediates (Chapter 4).

5.3.1 Absorption spectra at anodic and cathodic potentials

Fig. 5.2 displays XANES spectra of the studied nanoparticles at both anodic and cathodic potentials. The same spectra are shown in a wider energy range in Fig. B.3.

We will first focus on the spectra taken at anodic potentials (Fig. 5.2 **b**), because these spectra can be compared with previous HERFD-XANES studies for Pt nanoparticle oxidation. The spectra in Fig. 5.2 **b** gradually shift towards more positive energies as the electrode potential increases. This shift is well documented and is related to interactions between the Pt particles and oxygen.[22–26] The small initial shift between 0.4 and 0.9 V *vs.* RHE is subtle and corresponds to the adsorption of oxygen-containing species, such as *OH,[42,43] onto the electrode.[22] The more substantial shifts at more anodic potentials correspond to oxidation of the surface and the formation of platinum oxides.[22]

The aforementioned shifts are accompanied by the formation of a shoulder between 11567.5 and 11570 eV. This shoulder is located approximately 2 eV above the white line absorption peak and therefore likely corresponds to the formation of α-PtO_2:[26] the most likely oxide phase for thermally and electrochemically oxidized platinum.[23,44,45]

Interestingly, this shoulder is smaller in magnitude than previously reported peaks for electrochemically oxidized platinum nanoparticles and monolayers.[22–26] We ascribe this difference to a significant amount of Pt atoms remaining un-oxidized in the current

experiment. Oxidation of the nanoparticles was therefore likely restricted to the outer nanoparticle shell. This could partly be due to the difference between our 10 M NaOH electrolyte and the 0.01–0.1 M $HClO_4$ electrolytes used in previous literature experiment. However, the most probable reason for the lower degree of oxidation is a difference in nanoparticle size. Our particles are likely between 6 and 11 nm in size,[46] which is much larger than the previously studied 1.2 nm particles.[25] Our particles therefore possess a much lower surface-to-bulk atom ratio and, thus, are not oxidized as much as smaller nanoparticles, monolayers and nano-islands.[22–26] Nonetheless, the particles studied here exhibit detectable shifts in the absorption spectrum that match the available literature. This confirms that the current setup is sensitive towards changes in the platinum oxidation state.

After confirming that the current system can reproduce the known oxidative behavior of Pt, we can now explore the spectral changes under cathodic potentials. These results are shown in Fig. 5.2 **a**. In this panel, the most positive spectrum was recorded at 0 V *vs.* RHE. This spectrum overlaps well with the spectrum at 0.4 V *vs.* RHE, as can be seen in Fig. B.4. Though both spectra are rather similar, the spectrum at 0 V *vs.* RHE has a slightly lower white line intensity and is slightly broader than the spectrum at 0.4 V *vs.* RHE. This subtle broadening is due to adsorbed hydrogen, which covers 60 to 100% of the electrode surface at 0 V *vs.* RHE:[42,47–49] electrochemically adsorbed hydrogen broadens the XANES spectrum of platinum.[24,25] The broadening observed in Fig. B.4 is more subtle than the previously reported broadening, which again indicates a lower surface sensitivity due to a larger nanoparticle size in the current experiments.

The broadening in Fig. B.4 is also present at more cathodic potentials (Fig. 5.2 **a**). However, more cathodic potentials also cause a constant and small positive absorption edge shift. This edge shift appears subtle, yet consistent.

5.3.2 Difference spectra

To emphasize changes in the absorption edge, difference XANES spectra were created. Such spectra have previously been used to detect adsorbed species on Pt.[19,20] In the present case, difference spectra were obtained by subtracting the XANES spectrum at 0.4 V *vs.* RHE from the other spectra. The result of this data treatment is presented in Fig. 5.3.

We will first comment on changes in the Pt difference spectrum at anodic potentials (Fig. 5.3 **b**). At moderate anodic potentials (0.9 V), the small positive peak in the differ-

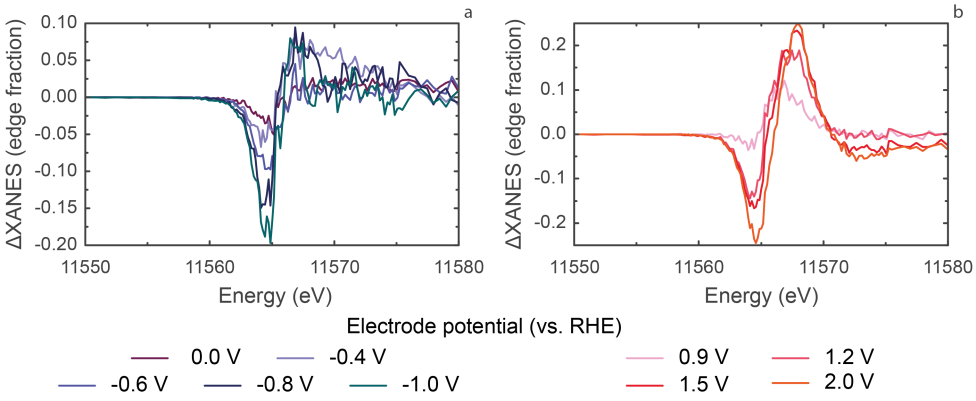

Fig. 5.3 | Difference spectra of electrodes polarized at cathodic potentials **(a)** and anodic potentials **(b)**. The reference spectrum for background subtraction was recorded at an applied potential of 0.4 *V vs.* RHE.

ence spectrum corresponds to a small shoulder in the normal spectrum (Fig. 5.2 **b**) that corresponds to the adsorption of *O or *OH.[22] At more anodic potentials, the growth of this peak is accompanied by a negative feature in the difference spectrum. This negative feature matches the corresponding edge shift in the normal XANES spectrum upon oxidation of the Pt nanoparticles. These negative and positive features in the difference spectra therefore facilitate the observation of more subtle features in the absolute absorption spectrum.

This enhancement also applies to spectra obtained at cathodic potentials, for which difference spectra are shown in Fig. 5.3 **a**. In these spectra, a negative peak is present at and below 0 *V vs.* RHE. This negative feature gradually develops at more cathodic potentials. At the most cathodic potentials, the negative feature appears to be accompanied by a positive feature between 11566 and 11567 *eV*. A more quantitative analysis is necessary to determine whether this positive feature is related to actual spectral changes, or rather due to random fluctuations in the absorption spectra.

5.3.3 Peak fitting

To quantitatively assess the data, we fitted several peaks to the spectra. Specifically, we fitted one pseudo-Voigt function at lower energies to account for the white line and one peak at higher energies to account for broadening of the spectra. These peaks will be referred to as the 'low-energy peak' and the 'high-energy peak', respectively. When fitting

these peaks, we accounted for the edge jump by including an arctangent function in the fitting procedure. This procedure and the fit parameters were based on a previous study of electrochemical Pt oxidation;[25] more details, all fit results and four representative fits are given in Appendix B. A summary of the fit results is given in Fig. 5.4. This figure presents the area of each of the peaks and the area of the sum of these peak, as a function of the applied potential.

In Fig. 5.4, the highest area is consistently found for the low-energy peak. This peak was previously ascribed to metallic Pt.[25] As such, Fig. 5.4 confirms that a significant part of the Pt nanoparticles remains metallic during the electrochemical experiments. The highest amount of metallic platinum is found at $0.4\ V$ *vs.* RHE. This is the expected state for Pt at this potential.[50]

At more anodic potentials, the area of the low-energy peak decreases, while the area of the high-energy peak increases. This increase of the high-energy peak agrees well with the oxidation of platinum, because this peak is located at energies where platinum oxides are generally observed.[22–26] The high-energy peak increase coincides with an increased sum of the peak areas. This peak area sum can be used as an indicator of the empty d-states and, by extension, the Pt oxidation state.[25] The increase of this peak therefore corresponds well with the expected oxidation of Pt at anodic potentials.

Accordingly, the peak sum decreases subtly at cathodic potentials. This has been observed before at $-0.04\ V$ *vs.* RHE in $0.1\ M$ $HClO_4$[25] and would suggest some degree of d-band filling with respect to Pt at $0.4\ V$ *vs.* RHE. Interestingly, the subtle decrease in sum peak area is accompanied by a decrease in the low-energy peak and an increase in the high-energy peak area. This indicates that the white line decrease and peak broadening in Fig. 5.2 are indeed caused by changes in the chemical nature of the Pt electrode.

5.3.4 Modeled XANES spectra

To explore these chemical changes, HERFD-XANES spectra were modeled using the OCEAN package.[29,30] We first modeled Pt and α-PtO_2 spectra for comparison with the known anodic behavior of Pt. We then additionally modeled spectra of two candidate ternary metal hydrides: Na_2PtH_4 and Na_2PtH_6. These hydrides were chosen based on the suggestion of their existence in Chapter 4. The resulting calculated X-ray absorption spectra and corresponding difference spectra are plotted in Fig. 5.5. In this figure, Panel **a** features an energy range that matches the energy range in Fig. 5.2; expanded spectra are shown in Fig. B.6.

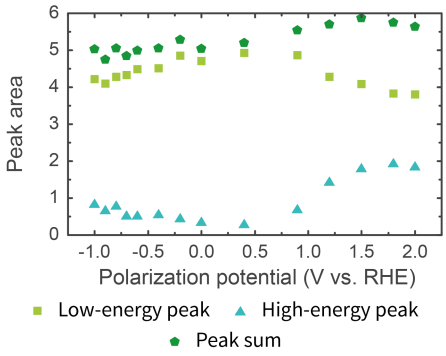

Fig. 5.4 | Areas of the fitted low-energy peak, high-energy peak and the sum of both peaks. Full fit results are given in Appendix B.

For assessing the quality of the modeled spectra, it is instructive to evaluate the difference between Pt and PtO_2. This assessment is facilitated by aligning the first inflection point of the modeled Pt absorption edge with that of the experimental spectrum at 0.4 *V vs.* RHE. The relative shift in the white line maximum between our Pt and α-PtO_2 models is 1.6 *eV*, which agrees well with the $\sim$ 2 *eV* shift observed experimentally. Our modeled Pt spectra also reproduce the positions of the various peaks in the experimental absorption spectrum, although the normalized intensity of peak features is overestimated. Finally, the difference spectrum of PtO_2 with a Pt background matches the anodic difference spectra in Fig. 5.2 **b** reasonably well: it crosses zero at 11565.6 *eV* (compared to our experimental 11565.3–11566.0 *eV*), and its peaks are 2.2 *eV* apart (compared to the experimental 3.1–3.4 *eV*). Based on these comparisons, our OCEAN simulations reasonably reproduce the experimental reference spectra.

Having established the applicability of our simulations, we will compare the theoretically modeled spectra for Na_2PtH_4 and Na_2PtH_6 with those of Pt. This comparison indicates that both hydrides have edge positions that are positive of the Pt edge position. Both hydrides also exhibit a white line peak, about 2.2–2.4 *eV* above that of Pt. Thirdly, both hydrides have isobestic points with Pt, at about 11567.2 *eV* (Na_2PtH_4 and 11566.6 *eV* (Na_2PtH_6). These isobestic points correspond to x-axis intercepts at the same positions in the difference spectra (Fig. 5.5 **b**). These difference spectra also contain a well-developed negative peak for both hydrides. A sharp positive peak is only present for Na_2PtH_6, after which the difference spectra slowly decreases to 0 at 11580 *eV*. In contrast, a broader positive peak is present for Na_2PtH_4. These features will be compared

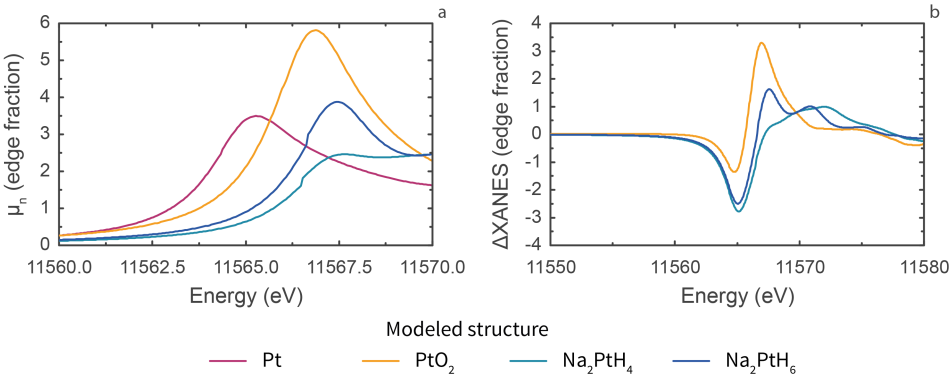

Fig. 5.5 | Modeled HERFD-XANES spectra **(a)** and difference spectra **(b)** for bulk Pt, PtO_2, $NaPtH_4$ and Na_2PtH_6. The reference spectrum for background subtraction in Panel **b** is the modeled spectrum for bulk Pt.

with the experimental difference spectra in the Discussion section.

5.3.5 Discussion

We established that the spectra of our Pt nanoparticles shift positive and a high-energy shoulder develops as the nanoparticles are partly oxidized to α-PtO_2. The observed behavior of the nanoparticles is consistent with previous literature reports and supports the validity of the spectral changes at cathodic potentials.

Under cathodic polarization, the Pt L_{III} XANES (Fig. 5.2 **a**) show a small positive edge shift and subtle whiteline decrease; Fig. 5.3 **a** emphasizes this shift at all cathodic potentials. These difference spectra also reveal a small shoulder above $11566\ eV$. Though the shape of this shoulder is affected by the formation of hydrogen bubbles during cathodic corrosion, the peak appears to be a significant feature of the data. This is indicated by Fig. 5.4, in which a constantly increasing high-energy peak is required to fit the cathodic XANES spectra.

It would be appealing to ascribe these changes to additional adsorbed hydrogen at more cathodic potentials; such "overpotential adsorbed hydrogen" (H_{OPD}) has been detected at cathodic potentials through vibrational spectroscopy.[12,49] The presence of H_{OPD} might even be inferred by the difference spectra (Fig. 5.3 **a**), which have similarly shaped difference spectra of Pt nanoparticles in a H_2 atmosphere.[19,20] However, adsorbed H_{OPD} does not appear consistent with the experimental observations upon closer inspection of the presented data. Specifically, the shape of the difference spectra appears

quantitatively different from those of hydrogen-covered Pt nanoparticles.[19,20] For these previously studied particles, the difference spectra indeed contain a positive and negative peak, but the peaks are approximately 6 eV apart and equal in magnitude. This contrasts with the peaks in Fig. 5.3, for which the negative peak can be more than twice as intense as the broad positive feature and the peaks are located more closely to each other.

A perhaps even more important observation is the magnitude of the observed difference spectra. For instance, the difference spectrum for 0 V *vs.* RHE (Fig. 5.3 **a**) corresponds to adsorption of 0.6 to 1 monolayer of hydrogen. This spectrum is much more subtle than those at the most cathodic potentials, which have magnitudes up to 4.5 times as high. Similarly, the high-energy peak in Fig. 5.4 increases in area from 0.33 ± 0.05 to 0.81 ± 0.09. If these changes were caused by H_{OPD} alone, the coverage would have to be in the order of several monolayers.

Therefore, it seems useful to explore alternative chemical species and compare the spectra in Fig. 5.3 to the modeled ternary metal hydride spectra in Fig. 5.5. At first glance, the Na_2PtH_6 spectrum in Fig. 5.5 appears most similar to the data. We therefore calculated linear combinations of the Pt and Na_2PtH_6 spectra to approximate nanoparticles that may be partly converted to Na_2PtH_6 during cathodic corrosion. These spectra were then converted into difference spectra by subtracting the modeled Pt spectrum from Fig. 5.5. An exemplary difference spectrum is plotted alongside two experimental spectra in Fig. 5.6.

The modeled difference spectrum in Fig. 5.6 corresponds to a linear combination of 94% Pt and 6% Na_2PtH_6. This difference spectrum matches the experimental cathodic spectra relatively well: it reproduces the difference between the negative and positive peak, the intensity ratio between both peaks, and the gradual decrease of the positive feature at higher absorption energies. The model spectrum might therefore be a reasonable approximation of Pt nanoparticles during cathodic corrosion in 10 M NaOH.

The match between the data and modeled spectra in Fig. 5.6 and the arguments preceding this figure provide important indications towards the existence of a ternary metal hydride during cathodic corrosion. However, two considerations prevent us from conclusively claiming the presence of a hydride like Na_2PtH_6. Firstly, our current theoretical efforts do not contain a modeled spectrum of adsorbed hydrogen on Pt. Such a spectrum would be essential in a systematic comparison of model candidate reaction intermediates. OCEAN calculations regarding these spectra are currently being performed and will be reported when they are finished. Secondly, the current experiments are not immune to

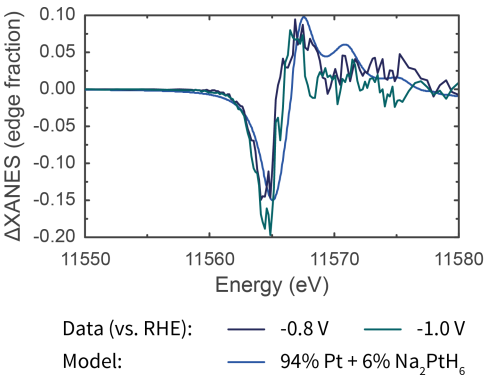

Fig. 5.6 | Difference spectra of electrodes polarized at -0.8 and -1.0 *V vs.* RHE. These spectra are plotted alongside a difference spectrum that is a linear combination of 94% of the modeled Pt spectrum and 6% of the modeled Na_2PtH_6 spectrum. For the data, the reference spectrum was that at 0.4 *V vs.* RHE. For the model, the reference spectrum is the modeled spectrum for pure Pt.

the effects of hydrogen bubbles. Though the use of a flow cell has significantly improved the signal-to-noise ratio when compared to initial experiments in a hanging-meniscus cell, the effect of bubbles is still visible in the presented spectra. These detrimental effects are amplified in further analysis using difference XANES spectra. The presented results might be improved by repeating them with samples that produce larger relative changes in the absorption spectrum. Such larger changes would then be more clearly distinguishable from noise due to hydrogen bubble formation. These pronounced changes could be achieved by using smaller nanoparticles, which should produce more clearly distinguishable spectral features.[25]

5.4 Conclusions

The current chapter has presented an *operando* HERFD-XANES investigation of Pt nanoparticles during cathodic corrosion. The chapter first established the proper functioning of the working setup by reproducing reported results on the anodic oxidation of Pt. After doing so, the cathodic behavior of Pt was studied.

This study of cathodically polarized Pt established a gradual shift in the Pt L_{III} absorption edge. This shift was accompanied by a shoulder at higher absorption energies. These changes were corroborated by further analysis using difference absorption spec-

tra and a peak fitting procedure. These results could then be compared to first principles calculations of XANES spectra of ternary metal hydrides. From these simulated spectra, the spectrum of the Na_2PtH_6 model reproduced several key features in the experimental absorption spectra.

Though further theoretical computations of hydrogen-covered Pt are necessary and experiments with smaller nanoparticles would be desirable, the current results provide the first experimental indications of the existence of Na_2PtH_6 during cathodic corrosion. If proven correct, the presence of Na_2PtH_6 would, to our knowledge, be the first report of such ternary metal hydrides at the water-platinum interface. The presented results are therefore relevant for both cathodic corrosion and electrochemistry as a whole.

5.5 Acknowledgements

Operando HERFD-XANES experiments were performed at SSRL, under proposal number 4751. Use of the Stanford Synchrotron Radiation Lightsource, SLAC National Accelerator Laboratory, is supported by the U.S. Department of Energy, Office of Science, Office of Basic Energy Sciences under Contract No. DE-AC02-76SF00515. The SSRL Structural Molecular Biology Program is supported by the DOE Office of Biological and Environmental Research, and by the National Institutes of Health, National Institute of General Medical Sciences (including P41GM103393). The contents of this chapter are solely the responsibility of the authors and do not necessarily represent the official views of NIGMS or NIH.

References

1. Haber, F. The Phenomenon of the Formation of Metallic Dust from Cathodes. *Transactions of the American Electrochemical Society* **2,** 189–196 (1902).
2. Yanson, A. I. *et al.* Cathodic Corrosion: A Quick, Clean, and Versatile Method for the Synthesis of Metallic Nanoparticles. *Angewandte Chemie International Edition* **50,** 6346–6350 (2011).
3. Yanson, Y. I. & Yanson, A. Cathodic corrosion. I. Mechanism of corrosion via formation of metal anions in aqueous medium. *Low Temperature Physics* **39,** 304–311 (2013).
4. Yanson, A., Antonov, P., Rodriguez, P. & Koper, M. Influence of the electrolyte concentration on the size and shape of platinum nanoparticles synthesized by cathodic corrosion. *Electrochimica Acta* **112,** 913–918 (2013).
5. Rodriguez, P., Tichelaar, F. D., Koper, M. T. M. & Yanson, A. I. Cathodic Corrosion as a Facile and Effective Method To Prepare Clean Metal Alloy Nanoparticles. *Journal of the American Chemical Society* **133,** 17626–17629 (2011).
6. Bennett, E. *et al.* A Synthetic Route for the Effective Preparation of Metal Alloy Nanoparticles and Their Use as Active Electrocatalysts. *ACS Catalysis* **6,** 1533–1539 (2016).
7. Kromer, M. L. *et al.* High-Throughput Preparation of Metal Oxide Nanocrystals by Cathodic Corrosion and Their Use as Active Photocatalysts. *Langmuir* **33,** 13295–13302 (2017).

8. Feng, J. *et al.* Cathodic Corrosion of a Bulk Wire to Nonaggregated Functional Nanocrystals and Nanoalloys. *ACS Applied Materials & Interfaces* **10,** 9532–9540 (2018).
9. Lawrence, M. J. *et al.* Electrochemical Synthesis of Nanostructured Metal-Doped Titanates and Investigation of Their Activity as Oxygen Evolution Photoanodes. *ACS Applied Energy Materials,* acsaem.8b00873 (2018).
10. Diaz-Morales, O., Hersbach, T. J. P., Badan, C., Garcia, A. C. & Koper, M. T. Hydrogen adsorption on nano-structured platinum electrodes. *Faraday Discussions* **210,** 301–315 (2018).
11. Nichols, R. & Bewick, A. Spectroscopic identification of the adsorbed intermediate in hydrogen evolution on platinum. *Journal of Electroanalytical Chemistry and Interfacial Electrochemistry* **243,** 445–453 (1988).
12. Jiang, Y.-X. *et al.* Characterization of surface water on Au core Pt-group metal shell nanoparticles coated electrodes by surface-enhanced Raman spectroscopy. *Chemical Communications,* 4608 (2007).
13. Wu, D.-Y., Li, J.-F., Ren, B. & Tian, Z.-Q. Electrochemical surface-enhanced Raman spectroscopy of nanostructures. *Chemical Society Reviews* **37,** 1025 (2008).
14. Dietzel, P. & Jansen, M. Synthesis and crystal structure determination of tetramethylammonium auride. *Chemical Communications* **21,** 2208–2209 (2001).
15. Long, G. & Grandjean, F. in *Comprehensive Coordination Chemistry II* 269–277 (Elsevier, 2003).
16. Calvin, S. *XAFS for Everyone* 1st ed. **1,** 427 (CRC Press, Boca Raton, FL, 2013).
17. Samant, M. G. & Boudart, M. Support effects on electronic structure of platinum clusters in Y zeolite. *The Journal of Physical Chemistry* **95,** 4070–4074 (1991).
18. Ichikuni, N. & Iwasawa, Y. In situ d electron density of Pt particles on supports by XANES. *Catalysis Letters* **20,** 87–95 (1993).
19. Behafarid, F. *et al.* Electronic properties and charge transfer phenomena in Pt nanoparticles on γ-Al2O3: size, shape, support, and adsorbate effects. *Physical Chemistry Chemical Physics* **14,** 11766 (2012).
20. Small, M. W., Sanchez, S. I., Marinkovic, N. S., Frenkel, A. I. & Nuzzo, R. G. Influence of Adsorbates on the Electronic Structure, Bond Strain, and Thermal Properties of an Alumina-Supported Pt Catalyst. *ACS Nano* **6,** 5583–5595 (2012).
21. Frenkel, A. I. *et al.* An in Situ Study of Bond Strains in 1 nm Pt Catalysts and Their Sensitivities to Cluster–Support and Cluster–Adsorbate Interactions. *The Journal of Physical Chemistry C* **117,** 23286–23294 (2013).
22. Friebel, D. *et al.* In situ X-ray probing reveals fingerprints of surface platinum oxide. *Phys. Chem. Chem. Phys.* **13,** 262–266 (2011).
23. Friebel, D., Miller, D. J., Nordlund, D., Ogasawara, H. & Nilsson, A. Degradation of Bimetallic Model Electrocatalysts: An In Situ X-Ray Absorption Spectroscopy Study. *Angewandte Chemie International Edition* **50,** 10190–10192 (2011).
24. Friebel, D. *et al.* Balance of Nanostructure and Bimetallic Interactions in Pt Model Fuel Cell Catalysts: In Situ XAS and DFT Study. *Journal of the American Chemical Society* **134,** 9664–9671 (2012).
25. Merte, L. R. *et al.* Electrochemical Oxidation of Size-Selected Pt Nanoparticles Studied Using in Situ High-Energy-Resolution X-ray Absorption Spectroscopy. *ACS Catalysis* **2,** 2371–2376 (2012).
26. Cui, Y.-T. *et al.* Wetting Induced Oxidation of Pt-based Nano Catalysts Revealed by In Situ High Energy Resolution X-ray Absorption Spectroscopy. *Scientific Reports* **7,** 1482 (2017).
27. Sokaras, D. *et al.* A seven-crystal Johann-type hard x-ray spectrometer at the Stanford Synchrotron Radiation Lightsource. *Review of Scientific Instruments* **84,** 053102 (2013).
28. Ravel, B. & Newville, M. ATHENA , ARTEMIS , HEPHAESTUS: data analysis for X-ray absorption spectroscopy using IFEFFIT. *Journal of Synchrotron Radiation* **12,** 537–541 (2005).
29. Vinson, J., Rehr, J. J., Kas, J. J. & Shirley, E. L. Bethe-Salpeter equation calculations of core excitation spectra. *Physical Review B* **83,** 115106 (2011).
30. Gilmore, K. *et al.* Efficient implementation of core-excitation Bethe–Salpeter equation calculations. *Computer Physics Communications* **197,** 109–117 (2015).
31. Kohn, W. & Sham, L. J. Self-Consistent Equations Including Exchange and Correlation Effects. *Physical Review* **140,** A1133–A1138 (1965).

32. Schwartz, C. P. *et al.* Temperature and radiation effects at the fluorine K-edge in LiF. *Journal of Electron Spectroscopy and Related Phenomena* **218,** 30–34 (2017).
33. Giannozzi, P. *et al.* QUANTUM ESPRESSO: a modular and open-source software project for quantum simulations of materials. *Journal of Physics: Condensed Matter* **21,** 395502 (2009).
34. Shirley, E. L. Optimal basis sets for detailed Brillouin-zone integrations. *Physical Review B* **54,** 16464–16469 (1996).
35. Perdew, J. P., Burke, K. & Ernzerhof, M. Generalized Gradient Approximation Made Simple. *Physical Review Letters* **77,** 3865–3868 (1996).
36. Perdew, J. P., Burke, K. & Ernzerhof, M. Generalized Gradient Approximation Made Simple [Phys. Rev. Lett. 77, 3865 (1996)]. *Physical Review Letters* **78,** 1396–1396 (1997).
37. Swanson, H. E. & Tatge, E. *Standard X-ray Diffraction Powder Patterns* (eds Swanson, H. E. & Tatge, E.) (U.S. Government Printing Office, Washington, 1953).
38. McBride, J. R., Graham, G. W., Peters, C. R. & Weber, W. H. Growth and characterization of reactively sputtered thin-film platinum oxides. *Journal of Applied Physics* **69,** 1596–1604 (1991).
39. Bronger, W., Müller, P., Schmitz, D. & Spittank, H. Synthese und Struktur von Na2PtH4, einem ternären Hydrid mit quadratisch planaren PtH42-Baugruppen. *Zeitschrift für anorganische und allgemeine Chemie* **516,** 35–41 (1984).
40. Ghebouli, M. *et al.* Theoretical prediction of the fundamental properties for the ternary Li2PtH6 and Na2PtH6. *Journal of Solid State Chemistry* **196,** 498–503 (2012).
41. Shirley, E. L. Local screening of a core hole: A real-space approach applied to hafnium oxide. *Ultramicroscopy* **106,** 986–993 (2006).
42. McCrum, I. T., Hickner, M. A. & Janik, M. J. First-Principles Calculation of Pt Surface Energies in an Electrochemical Environment: Thermodynamic Driving Forces for Surface Faceting and Nanoparticle Reconstruction. *Langmuir* **33,** 7043–7052 (2017).
43. Chen, X., McCrum, I. T., Schwarz, K. A., Janik, M. J. & Koper, M. T. M. Co-adsorption of Cations as the Cause of the Apparent pH Dependence of Hydrogen Adsorption on a Stepped Platinum Single-Crystal Electrode. *Angewandte Chemie International Edition* **56,** 15025–15029 (2017).
44. Miller, D. J. *et al.* Oxidation of Pt(111) under Near-Ambient Conditions. *Physical Review Letters* **107,** 195502 (2011).
45. Huang, Y.-F., Kooyman, P. J. & Koper, M. T. M. Intermediate stages of electrochemical oxidation of single-crystalline platinum revealed by in situ Raman spectroscopy. *Nature Communications* **7,** 12440 (2016).
46. Yanson, A., Antonov, P., Yanson, Y. & Koper, M. Controlling the size of platinum nanoparticles prepared by cathodic corrosion. *Electrochimica Acta* **110,** 796–800 (2013).
47. Koper, M. T. & Lukkien, J. J. Modeling the butterfly: the voltammetry of $(\sqrt{3} \times \sqrt{3})$R30° and p$(2 \times 2)$ overlayers on (111) electrodes. *Journal of Electroanalytical Chemistry* **485,** 161–165 (2000).
48. Garcia-Araez, N., Lukkien, J. J., Koper, M. T. & Feliu, J. M. Competitive adsorption of hydrogen and bromide on Pt(100): Mean-field approximation vs. Monte Carlo simulations. *Journal of Electroanalytical Chemistry* **588,** 1–14 (2006).
49. Jerkiewicz, G. Electrochemical Hydrogen Adsorption and Absorption. Part 1: Under-potential Deposition of Hydrogen. *Electrocatalysis* **1,** 179–199 (2010).
50. Pourbaix, M. *Atlas of electrochemical equilibria in aqueous solutions* 2nd ed., 644 (National Association of Corrosion Engineers, 1974).